

Data-driven reduced order model for residence time distribution analysis of an industrial-scale continuous casting tundish

Harshith Gowrachari^{*1}, Mattia Giuseppe Barra^{†3}, Giovanni Stabile^{‡2},
Gianluca Bazzaro^{§3}, and Gianluigi Rozza^{¶1}

¹Mathematics Area, mathLab, International School for Advanced Studies,
via Bonomea 265, 34136, Trieste, Italy.

²Biorobotics Institute, Sant'Anna School of Advanced Studies,
V.le R. Piaggio 34, 56025, Pontedera, Pisa, Italy.

³Danieli Research Center, Danieli & C. S.p.A., Via Nazionale 41, 33042 ,
Buttrio, Province of Udine, Italy.

Abstract

The continuous casting tundish plays a critical role as a metallurgical reactor in the continuous casting process, with its flow characteristics serving as a key parameter in the production of high-quality steel. These characteristics are typically assessed through residence time distribution (RTD) curves. This study examines the flow behaviour in a single-strand continuous casting tundish through a combination of numerical simulations and experimental validation. Steady-state full order model (FOM) simulations are performed under both isothermal and non-isothermal conditions to evaluate the influence of thermal buoyancy on the velocity field, which is found to be negligible. The resulting flow fields are used to initialize transient tracer transport simulations for determining the RTD and flow volume partitioning. Subsequently, a data-driven reduced order model (ROM) is developed to predict the RTD response. Comparison of RTD curves obtained from experiments, FOM, and ROM shows excellent agreement, with the ROM accurately capturing the key flow characteristics at a fraction of the computational cost. These results highlight the potential of ROM techniques for efficient real-time analysis, design, and optimization of tundish operations in metallurgical processes.

Keywords: continuous casting tundish; residence time distribution; computational fluid dynamics; data-driven reduced order model; digital twin.

1 Introduction

Continuous casting is an established method for solidifying molten steel into semi-finished products such as billets, blooms, and slabs, accounting for approximately 96% of global steel production [29]. A key component of this process is the tundish (see Figure 1), a refractory-lined vessel that receives molten steel from the ladle and delivers it to the mold for solidification. Historically, the tundish was viewed primarily as a passive buffer, bridging the discontinuous operations of secondary metallurgy, such as degassing, de-oxidation, alloying, temperature control, and cleanliness adjustments, with the continuous casting line, while also distributing steel

^{*}hgowrach@sissa.it

[†]m.barra@danieli.com

[‡]giovanni.stabile@santannapisa.it

[§]g.bazzaro@danieli.it

[¶]grozza@sissa.it

uniformly to multiple strands [17]. In recent decades, however, the tundish has evolved into an active metallurgical reactor, playing a central role in controlling flow dynamics, thermal gradients, and inclusion removal. Its influence on the cleanliness and quality of the final product has made it a critical focus of both design optimization and process control. The increasing demand for high-quality steel has intensified the focus on product cleanliness, which is largely governed by the presence of non-metallic inclusions [31]. These inclusions, whether endogenous or exogenous, can significantly impair the mechanical and corrosion properties of steel if not adequately removed during processing [25, 14]. Their size, shape, composition, and distribution affect critical performance metrics such as strength, toughness, fatigue life, and corrosion resistance. Minimizing inclusion content requires precise control over the steel, slag, and refractory chemistry, as well as fluid flow within each metallurgical vessel during secondary refining and continuous casting [32].

As the tundish is the final refining stage before solidification, its flow characteristics play a pivotal role in modifying inclusion content. Understanding and optimizing flow behavior within the tundish is therefore essential to achieving high product quality.

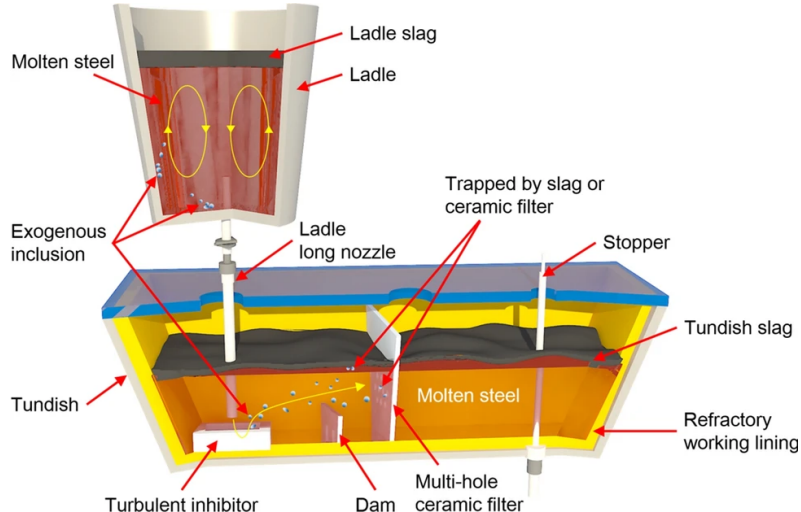


Figure 1: Schematic of a single-strand tundish (taken from [26]), illustrating key components and flow features. The diagram depicts multiphase interactions involving molten steel, slag, and inclusion flotation. Flow control devices, such as the impact pad (turbulence inhibitor) and dam, are also shown, highlighting their role in enhancing steel quality and casting performance.

A commonly employed method for characterizing molten steel flow in tundishes is the stimulus–response technique [27]. This involves injecting a tracer at the tundish inlet and monitoring its concentration at the outlet over time, yielding the residence time distribution (RTD) curve [18]. Step and pulse tracer inputs are typically used. In multi-strand tundishes, the global RTD is computed as a flow-weighted average of outlet-specific RTDs, accounting for unequal flow splits.

RTD analysis offers insights into flow behavior, including the detection of preferential flow paths, shortcuts that allow molten steel to exit with minimal residence time, and limiting the removal of non-metallic inclusions. These appear as early peaks in the RTD curve and are detrimental to steel cleanliness. Additionally, the RTD can quantify dead volume—regions where residence time exceeds twice the theoretical value, often associated with recirculation and stagnation. Excessive dead volume can reduce inclusion removal efficiency and increase the risk of steel freezing due to prolonged exposure.

RTD curves can be derived from both numerical and physical simulations. Physical modelling is often performed using full or reduced-scale water models, with water representing molten steel and a NaCl solution serving as the tracer [18, 6]. The tracer's physical properties and injection method, particularly its concentration, density, and volume, significantly impact measurement accuracy [12, 5, 2]. While lower tracer dosages help minimize flow disturbances, they must remain within the detection limits of the measurement equipment [4].

Accurate numerical prediction of RTD curves depends strongly on the turbulence model used to represent the fluid flow. Validation is typically performed by comparing simulation results with experimental data from water models [12].

Reduced order models (ROMs) offer computationally efficient alternatives to high-fidelity numerical simulations, mitigating their high computational cost [16]. For instance, evaluating RTD curves across multiple operating parameters using full-order models (FOMs) is computationally expensive, motivating for the ROMs capable of capturing the dominant dynamics across a range of parameters. In ROM construction, once a low-dimensional approximation subspace of the FOM solution manifold is obtained, the system dynamics must be evolved within this subspace. This is typically achieved by solving for modal coefficients or latent variables, using either intrusive or non-intrusive approaches.

In the intrusive approach, the discretized governing equations are projected onto the reduced subspace, yielding a system of reduced order ordinary differential equations (ODEs). This projection based approach is commonly referred to as Galerkin or Petrov–Galerkin ROM, is inherently physics-based [1, 20, 21, 11, 15]. However, this approach requires full access to the underlying equations and the internal data structures of the high-fidelity solver, including the discretized operators. Such dependencies often limit its applicability in industrial practice, where commercial solvers (software) are prevalent and source code is inaccessible. Furthermore, for non-linear or non-affine problems, intrusive methods may not provide significant computational gains [15].

In contrast, non-intrusive approaches are entirely data-driven and do not depend on the governing equations. These methods have demonstrated substantial speed-ups even for non-linear and non-affine problems [24]. Due to their flexibility and minimal implementation constraints, non-intrusive frameworks are particularly attractive in real-world applications.

This article extends the previous work on intrusive projection-based ROMs for RTD analysis [7]. In industries, the most common practice is to use commercial solvers for FOMs, which limits access to source code, rendering intrusive ROM development impractical. To overcome this limitation, we develop a non-intrusive, data-driven ROM [24, 8] for RTD analysis, as an alternative compatible with commercial solvers, yielding excellent accuracy across parametric variations, making it well-suited for industrial applications.

The main contributions of this work are as follows:

- We develop a non-intrusive data-driven ROM for RTD analysis in an industrial-scale, three-dimensional continuous casting tundish.
- The data-driven ROM results is validated against both experimental data and high-fidelity FOM simulations, demonstrating excellent accuracy.
- The ROM exhibits strong generalization capabilities for unseen parameter instances, showing good agreement with FOM results. The framework is computationally efficient and

scalable, making it suitable for real-time monitoring, optimization, and design-space exploration in continuous casting, thereby offering a practical tool to support advanced steelmaking operations.

This paper is organised as follows. Section 2 describes the full-order model, including the governing equations, turbulence modelling, Boussinesq approximation, species transport, and the numerical methods employed. In Section 3, the data-driven ROM framework is introduced, comprising the offline and online stages. Section 4 outlines the numerical setup, including the computational domain and boundary conditions. The results and discussion are presented in Section 5, and finally, conclusions and perspectives are discussed in Section 6.

2 Full order model

In this section, we present the physical and mathematical modelling approach for simulating isothermal and non-isothermal conditions during steady-state tundish operation, where the Reynolds-averaged Navier-Stokes (RANS) equations are employed. Further, we describe the transient tracer transport model employed for the evaluation of RTD curves.

2.1 Governing equations

The isothermal, incompressible turbulent flow within the tundish, where the working fluid is water, is governed by the continuity and momentum equations:

$$\nabla \cdot (\rho \mathbf{u}) = 0, \quad (1)$$

$$\rho(\mathbf{u} \cdot \nabla) \mathbf{u} = -\nabla P + \nabla \cdot \left[\mu_{\text{eff}} \left(\nabla \mathbf{u} + (\nabla \mathbf{u})^{\top} \right) \right] + \mathbf{F}, \quad (2)$$

$$\mu_{\text{eff}} = \mu + \mu_t = \mu + \rho c_{\mu} \frac{k^2}{\varepsilon}. \quad (3)$$

Here, \mathbf{u} is the velocity vector, P denotes pressure, and \mathbf{F} represents the body force. The effective viscosity μ_{eff} accounts for both the molecular viscosity μ and the turbulent eddy viscosity μ_t , the latter modelled via the standard $k - \varepsilon$ turbulence framework. The turbulence parameters k and ε are obtained from the transport equations for turbulent kinetic energy and its dissipation rate, respectively.

2.2 Boussinesq approximation

For non-isothermal flow conditions in the tundish, where the working fluid is molten steel, buoyancy effects arising from temperature-dependent density variations are incorporated via the Boussinesq approximation. Under this framework, the momentum equation becomes:

$$\rho(\mathbf{u} \cdot \nabla) \mathbf{u} = -\nabla P + \nabla \cdot \left[\mu_{\text{eff}} \left(\nabla \mathbf{u} + (\nabla \mathbf{u})^{\top} \right) \right] + \rho_{\text{ref}} \beta \Delta T \mathbf{g}, \quad (4)$$

where the buoyancy term $\rho_{\text{ref}} \beta \Delta T \mathbf{g}$ accounts for density variation due to temperature difference. Here, ρ_{ref} is a reference density, β the thermal expansion coefficient, $\Delta T = T - T_{\text{ref}}$ the temperature deviation from a reference temperature, and \mathbf{g} the gravitational acceleration vector.

This approximation assumes constant density in all governing equations, except in the buoyancy term of the momentum equation, where linear temperature dependence is retained:

$$(\rho - \rho_{\text{ref}}) \mathbf{g} \approx -\rho_{\text{ref}} \beta \Delta T \mathbf{g}. \quad (5)$$

The Boussinesq approximation is valid when temperature variations are moderate such that $\beta \Delta T \ll 1$. For fluids such as water or molten steel, where $\beta \sim 10^{-4} \text{ K}^{-1}$, this condition holds

for temperature differences up to 15–20 °C, yielding $\beta\Delta T \sim 10^{-3}$.

The transient temperature field is computed by solving the energy conservation equation:

$$\frac{\partial(\rho C_p T)}{\partial t} + \nabla \cdot (\rho C_p T \mathbf{u}) = \nabla \cdot (k_{\text{eff}} \nabla T), \quad (6)$$

where C_p is the specific heat at constant pressure, and k_{eff} is the effective thermal conductivity. The temperature field couples with the velocity field through the buoyancy term in equation (4). In the present simulations, all tundish walls and the free surface are assumed adiabatic, thereby neglecting heat flux through these boundaries.

2.3 Turbulence model

Turbulence is modelled using the standard eddy-viscosity based k - ε model [10]. This approach introduces two additional transport equations: one for the turbulent kinetic energy k , and another for its rate of dissipation ε , given by

$$\rho \mathbf{u} \cdot \nabla k = \nabla \cdot \left(\frac{\mu_{\text{eff}}}{\sigma_k} \nabla k \right) + G_k - \rho \varepsilon, \quad (7)$$

$$\rho \mathbf{u} \cdot \nabla \varepsilon = \nabla \cdot \left(\frac{\mu_{\text{eff}}}{\sigma_\varepsilon} \nabla \varepsilon \right) + C_1 \frac{\varepsilon}{k} G_k - C_2 \rho \frac{\varepsilon^2}{k}, \quad (8)$$

where G_k denotes the production of turbulent kinetic energy due to velocity gradients:

$$G_k = \mu_t \left(\nabla \mathbf{u} + (\nabla \mathbf{u})^\top \right) : \nabla \mathbf{u}.$$

The turbulent viscosity is computed as $\mu_t = \rho C_\mu \frac{k^2}{\varepsilon}$, and the model constants are: $C_\mu = 0.09$, $C_1 = 1.44$, $C_2 = 1.92$, $\sigma_k = 1.00$, and $\sigma_\varepsilon = 1.30$. For scalar transport, the turbulent Prandtl number is set to $\text{Pr}_t = 0.90$.

2.4 Species transport equation

The transient evolution of tracer concentration, represented as a mass fraction c_i , is computed by solving the species transport equation using the previously obtained velocity field:

$$\frac{\partial(\rho c_i)}{\partial t} + \nabla \cdot (\rho \mathbf{u} c_i) = \nabla \cdot (\rho D_{\text{eff}} \nabla c_i), \quad (9)$$

where ρ is the fluid density, and D_{eff} is the effective diffusivity, given by:

$$D_{\text{eff}} = D_m + D_t = D_m + \frac{\mu_{\text{eff}}}{\text{Pr}_t}. \quad (10)$$

Here, D_m is the molecular diffusivity, D_t is the turbulent (eddy) diffusivity, μ_{eff} is the effective viscosity defined previously, and Pr_t is the turbulent Prandtl number. The transport of species is assumed to be passive, i.e., it does not influence the flow field.

The numerical simulations are conducted using the finite-volume library OpenFOAM [28], an object-oriented C++ framework that supports modular formulation of the governing equations and facilitates solver customization. For steady-state, isothermal flow simulations, the incompressible solver simpleFoam is employed and for non-isothermal flow, the buoyantBoussinesqSimpleFoam solver is considered, which accounts for buoyancy effects under the Boussinesq approximation. Transient passive tracer transport is simulated using a customized solver, scalarTurbulentTransportFoam, which extends the standard scalarTransportFoam by incorporating

turbulent diffusivity in the scalar transport equation.

All flow solvers rely on the SIMPLE algorithm [3] to ensure iterative convergence of the pressure–velocity coupling, and, where applicable, the energy equation. The discretization schemes adopted in the finite-volume formulation are summarized in Table 1. Second-order accuracy is maintained for the majority of terms, while a first-order upwind scheme is applied to turbulence quantities to enhance numerical stability. For time integration in transient tracer simulations, a second-order implicit backward scheme is employed.

Term	Scheme
Time derivative	steadyState / Second-order implicit backward
Convective term (momentum)	Second-order upwind
Convective term (energy, species)	Second-order upwind
Convective term (turbulence: k, ε)	First-order upwind
Diffusive term (viscous, thermal)	Central differing
Gradient term	Limited linear construction

Table 1: Summary of numerical schemes considered for full-order simulations.

3 Reduced order model

This section presents the data-driven ROM framework for RTD analysis. The framework is divided into two stages: offline and online. In the offline stage, a ROM is constructed from high-fidelity simulation data. This involves generating full-order solution snapshots, extracting dominant flow structures using POD, and constructing a low-dimensional linear approximation subspace. The subsequent online phase enables rapid evaluation of the ROM for new parameter instances, with computational efficiency achieved via a regression-based approximation of the parameter-dependent modal coefficients.

3.1 Offline stage

To construct the reduced basis space, the high-fidelity model introduced in Section 2 is solved for a finite set of parameter values $\mathcal{K} = \{\boldsymbol{\mu}_k\}_{k=1}^{N_\mu} \subset \mathcal{P}$. Given the time-dependent nature of the problem, the snapshot collection must capture both parametric and temporal variability. Therefore, a discrete set of time instances $\{t_l\}_{l=1}^{N_t} \subset [0, T]$ is also defined. The total number of snapshots is then $N_s = N_\mu \cdot N_t$.

The snapshot matrix $\mathcal{S} \in \mathbb{R}^{N_h \times N_s}$ is assembled by collecting high-fidelity solutions of the tracer concentration field, evaluated at N_h spatial degrees of freedom for each parameter-time pair:

$$\mathcal{S} = \left[c(\boldsymbol{\mu}_1, t_1), \dots, c(\boldsymbol{\mu}_k, t_l), \dots, c(\boldsymbol{\mu}_{N_\mu}, t_{N_t}) \right]. \quad (11)$$

To generate a low-dimensional subspace suitable for projection-based model reduction, several techniques are available in the literature [13, 9, 16], including Proper Orthogonal Decomposition (POD), Proper Generalized Decomposition (PGD), and reduced basis (RB) methods based on greedy sampling. Among model order reduction techniques, POD is widely adopted for its ability to extract the most energetic modes from computational fluid dynamics (CFD) simulations [16]. In this work, we adopt the POD approach to construct the reduced basis. Specifically, a nested POD procedure is employed, where a first-stage POD is performed in the temporal domain, followed by a second-stage POD across the parametric dimension, as proposed

in [20, 16].

Let $c(\mu, t)$ denote a scalar or vector-valued field, with a corresponding collection of N_s snapshot realizations $\{c_i\}_{i=1}^{N_s}$. The goal of POD is to identify, for each desired reduced dimension $N_{\text{POD}} = 1, \dots, N_s$, an optimal set of orthonormal basis functions $\{\varphi_j\}_{j=1}^{N_{\text{POD}}}$ that best approximates the snapshots in the least-squares sense. Specifically, the POD basis minimizes the total projection error:

$$\min_{\{\varphi_j\}_{j=1}^{N_{\text{POD}}}} \sum_{i=1}^{N_s} \left\| c_i - \sum_{j=1}^{N_{\text{POD}}} \langle c_i, \varphi_j \rangle_{L^2(\Omega)} \varphi_j \right\|_{L^2(\Omega)}^2. \quad (12)$$

These basis functions must also satisfy the orthonormality condition:

$$\langle \varphi_i, \varphi_j \rangle_{L^2(\Omega)} = \delta_{ij}, \quad \forall i, j = 1, \dots, N_{\text{POD}}. \quad (13)$$

As shown in [13], the minimization problem in Eq. (12) is equivalent to solving the eigenvalue problem associated with the correlation matrix $\mathbf{C} \in \mathbb{R}^{N_s \times N_s}$, defined as:

$$\mathbf{C}\mathbf{Q} = \mathbf{Q}\Lambda, \quad (14)$$

$$\mathbf{C}_{ij} = \langle c_i, c_j \rangle_{L^2(\Omega)}, \quad \forall i, j = 1, \dots, N_s, \quad (15)$$

where \mathbf{Q} contains the eigenvectors and Λ is the diagonal matrix of eigenvalues $\{\lambda_i\}_{i=1}^{N_s}$. The POD basis functions are then reconstructed as a linear combination of the original snapshots:

$$\varphi_i = \frac{1}{\sqrt{\lambda_i}} \sum_{j=1}^{N_s} c_j (\mathbf{Q})_{ij}. \quad (16)$$

The POD basis functions obtained through the methodology described above define a reduced approximation subspace given by:

$$V_{\text{rb}} = \text{span} \{ \varphi_i \}_{i=1}^{N_{\text{rb}}} \subset L^2(\Omega), \quad (17)$$

where $N_{\text{rb}} \ll N_h$ is the dimension of the reduced basis space, typically determined by analyzing the decay of the associated POD eigenvalues.

Once the reduced subspace is identified, the high-fidelity concentration field $c(\mu, t)$ can be approximated by a linear combination of the POD modes:

$$c(\mu, t) \approx \sum_{i=1}^{N_{\text{rb}}} a_i(\mu, t) \varphi_i(x), \quad (18)$$

where $\{a_i(\mu, t)\}_{i=1}^{N_{\text{rb}}}$ denote the parameter-time dependent modal coefficients, and $\{\varphi_i(x)\}_{i=1}^{N_{\text{rb}}}$ are the orthonormal, parameter-time independent POD basis functions.

The reduced basis matrix $V_{\text{rb}} \in \mathbb{R}^{N_h \times N_{\text{rb}}}$ is formed by arranging the POD modes as column vectors. The corresponding reduced coefficients $a(\mu, t_i) \in \mathbb{R}^{N_{\text{rb}}}$ are computed by projecting the full-order solution $c(\mu, t_i) \in \mathbb{R}^{N_h}$ onto the reduced basis space:

$$a(\mu, t_i) = V_{\text{rb}}^\top c(\mu, t_i). \quad (19)$$

The POD basis is computed using the method of snapshots [19]. The basis generation is performed within the ITHACA-FV framework¹ [22], an OpenFOAM based library for reduced order modelling of parametrized problems.

¹The ITHACA-FV source code is available at <https://github.com/ITHACA-FV/ITHACA-FV>.

3.2 Online stage

To enable efficient prediction of solution snapshots for unseen parameter instances, it is necessary to construct a mapping from the parameter space to the space of reduced coefficients. This task involves approximating the solution manifold, represented in terms of parameter-time dependent modal coefficients associated with the reduced basis, using data from high-fidelity simulations.

Given a set of $N_s = N_\mu \cdot N_t$ input-output pairs $\{(t_l, \mu_k), a_{kl}\}_{k=1, l=1}^{N_\mu, N_t}$, where $a_{kl} \in \mathbb{R}^{N_{\text{rb}}}$ are the reduced coefficients computed via projection at time t_l and parameter μ_k , the goal is to approximate the mapping:

$$f : (t, \mu) \in \mathbb{R} \times \mathbb{R}^{d_\mu} \mapsto a(t, \mu) \in \mathbb{R}^{N_{\text{rb}}}. \quad (20)$$

Several techniques are available for learning the map s , including linear interpolation, radial basis function (RBF) interpolation [30, 23], Gaussian process regression (GPR), inverse distance weighting (IDW), multi-fidelity methods, and artificial neural networks (ANNs) [8, 24]. In this study, we primarily employ RBF interpolation due to its robustness and efficiency in moderately high-dimensional parameter spaces.

Once the mapping is trained, the reduced order solution for any unseen input pair (μ^*, t^*) is efficiently reconstructed as:

$$\tilde{c}(\mu^*, t^*) = \sum_{j=1}^{N_{\text{rb}}} f_j(\mu^*, t^*) \varphi_j(x), \quad (21)$$

where $f_j(\mu^*, t^*)$ is the predicted j -th modal coefficient, and $\{\varphi_j(x)\}_{j=1}^{N_{\text{rb}}}$ are the reduced basis functions. This enables accurate, low-cost approximations of the concentration field at new parameter instances.

4 Numerical setup

This section outlines the numerical framework employed for full-order model simulations. The computational geometry and mesh configuration of the tundish system are presented in Section 4.1, while the boundary conditions for both isothermal and non-isothermal cases are detailed in Section 4.2.

4.1 Computational domain

A three-dimensional computational domain is constructed based on a full-scale (1:1) industrial tundish, as illustrated in Figure 2, indicating inlet, outlet, and wall boundaries. The mesh was generated using snappyHexMesh in OpenFOAM, resulting in approximately 3.6 million cells. The mesh is predominantly composed of hexahedra (97%), with additional prism layers, pyramids, tetrahedra, and polyhedra near geometrically complex regions (Figure 3).

4.2 Boundary Conditions

A constant volumetric flow rate is prescribed at the inlet, outflow conditions are applied at the outlet, and no-slip conditions are enforced on all walls using standard wall functions. For non-isothermal simulations, lateral and bottom wall heat losses are set to 6 kW m^{-2} . A summary of input parameters and boundary conditions is provided in Table 2.

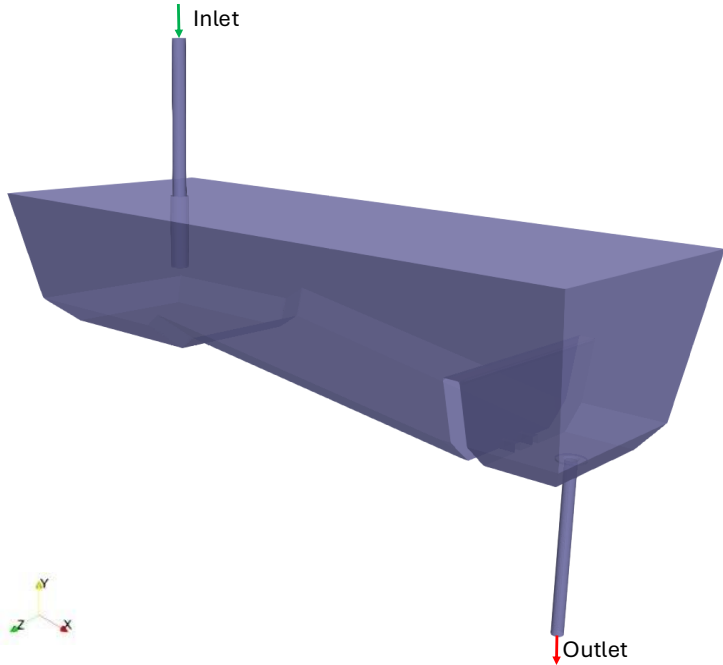


Figure 2: Isometric view of the computational domain for the 1:1 scaled single-strand tundish. The inlet and outlet locations are indicated; all remaining boundaries are considered as no-slip walls.

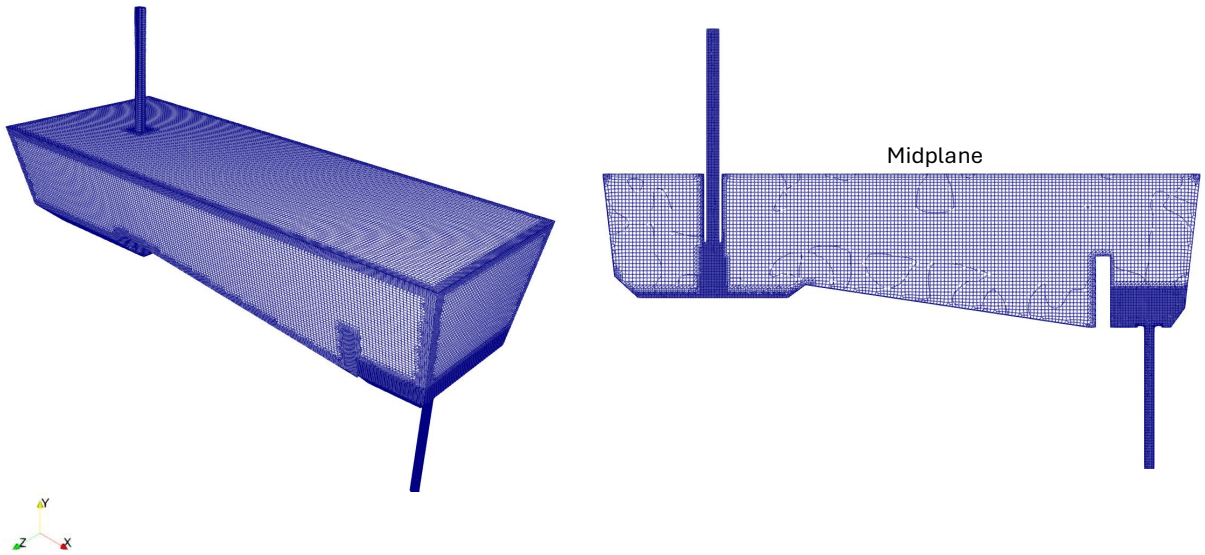


Figure 3: Discretized computational domain of a 1:1 scaled single-strand tundish. **Left:** Isometric view of the mesh; **Right:** 2D midplane slice showing mesh refinement near the inlet jet impingement region and outlet, and with six prism layers adjacent to the walls.

Two simulation scenarios are considered. First, an isothermal water case, leverages dynamic similarity (matched Froude number) to replicate molten steel flow characteristics and to validate the model against water experiments. Second, a non-isothermal molten steel case, incorporates buoyancy effects via the Boussinesq approximation to capture thermal stratification relevant to

industrial tundish operation. Together, these cases enable both model validation and demonstration under realistic continuous casting conditions.

Parameter	Water (Isothermal)	Molten steel (Non-isothermal)
Density	1000 kg/m^3	6900 kg/m^3
Kinematic viscosity	$1 \times 10^{-6} \text{ m}^2/\text{s}$	$0.8 \times 10^{-6} \text{ m}^2/\text{s}$
Reference pressure	$101,325 \text{ Pa}$	$101,325 \text{ Pa}$
Heat capacity	—	$800 \text{ J/kg} \cdot \text{K}$
Thermal conductivity	—	$35 \text{ W/m} \cdot \text{K}$
Thermal expansion coefficient	—	0.000127 K^{-1}
Inlet volumetric flow rate	$0.0102657 \text{ m}^3/\text{s}$	$0.0102657 \text{ m}^3/\text{s}$
Inlet velocity	1.6 m/s	1.6 m/s
Inlet temperature	—	1823.15 K
Wall (flow)	No-slip	No-slip
Wall (heat loss)	—	6 kW/m^2

Table 2: Summary of input parameters and boundary conditions used in the isothermal and non-isothermal simulations.

For tracer injection, a pulse input is applied by setting the tracer concentration (mass fraction) at the inlet to unity for $0 \leq t \leq 2 \text{ s}$, and zero thereafter. The outlet concentration is recorded over $0 \leq t \leq 3000 \text{ s}$ to generate the RTD curves (see Figure 4).

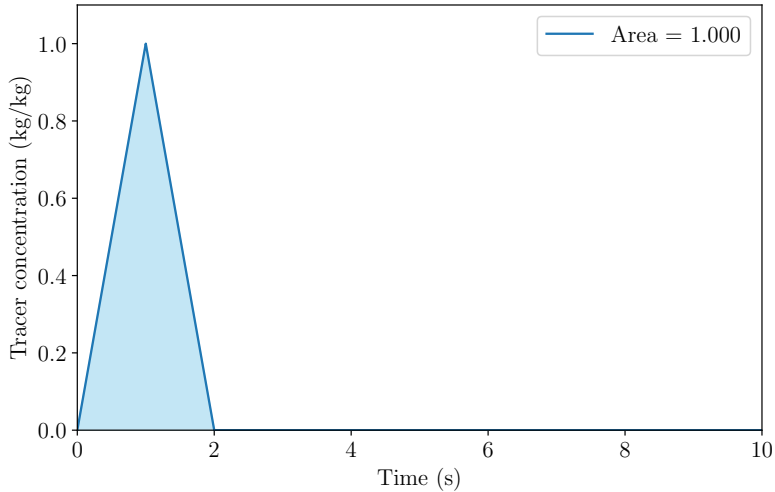


Figure 4: Time-dependent tracer concentration profile imposed at the inlet for the transient species transport simulation.

5 Results and discussion

In this study, three-dimensional steady-state simulations of turbulent flow are conducted under both isothermal (water) and non-isothermal (molten steel) conditions. To evaluate the spatial variation of the streamwise velocity component u_x , velocity profiles are extracted along selected horizontal and vertical lines within the tundish, as illustrated in Figure 5. Figure 6 compares the streamwise velocity distributions at various lateral (y) positions for the two thermal conditions, while Figure 7 presents corresponding profiles along vertical sections at different streamwise (x)

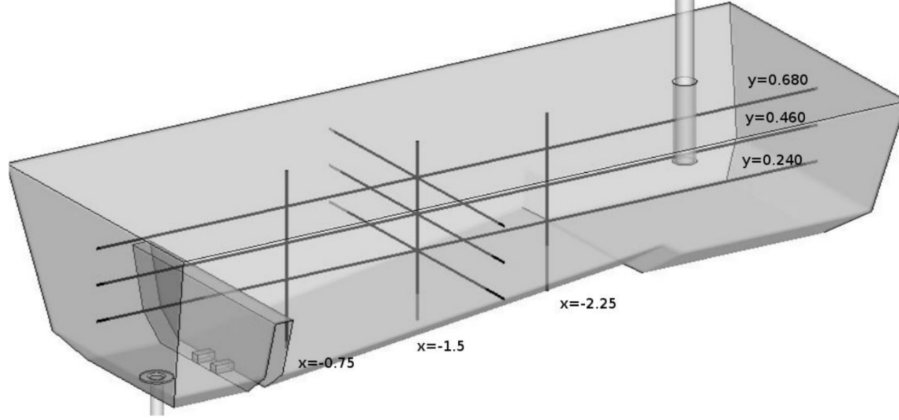


Figure 5: Positions of the horizontal and vertical lines along which streamwise velocity profiles are extracted within the tundish.

locations.

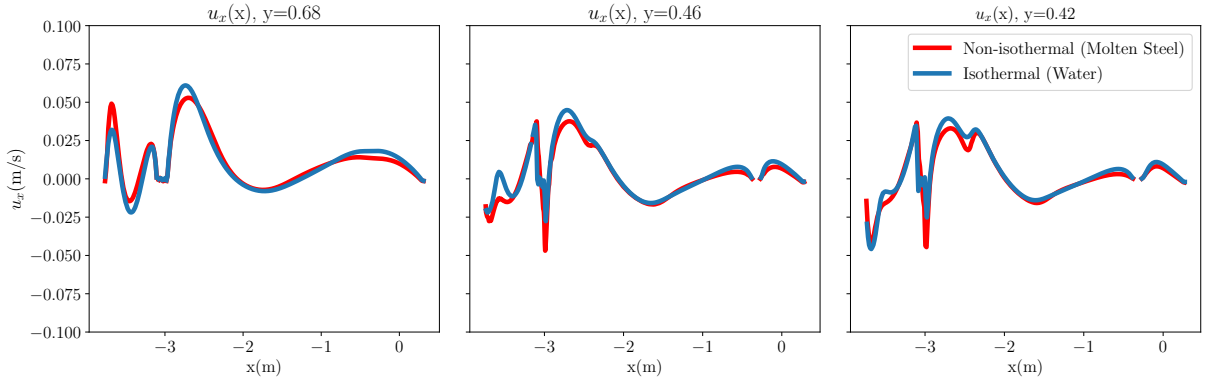


Figure 6: Distributions of streamwise velocity along horizontal lines at selected y -positions (illustrated in Figure 5), for both isothermal and non-isothermal cases.

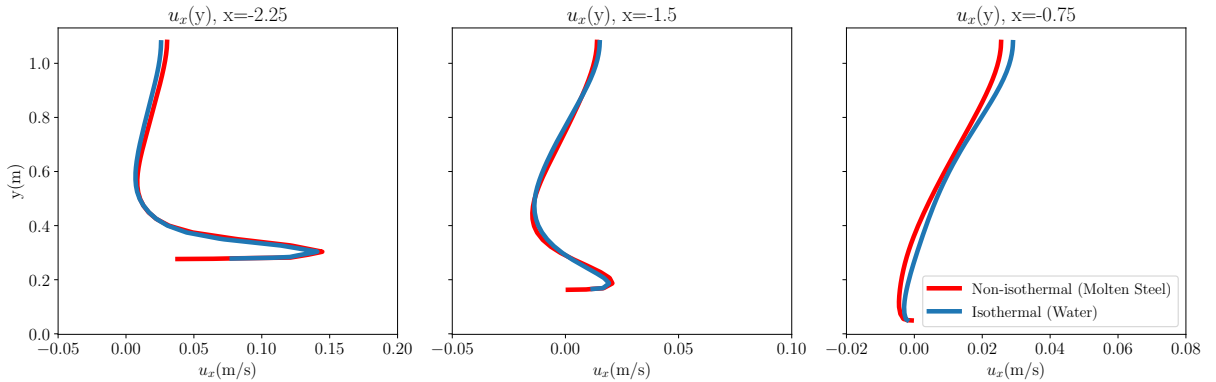


Figure 7: Distributions of streamwise velocity measured along vertical lines at selected x -positions (illustrated in Figure 5), for both isothermal and non-isothermal cases.

The velocity distributions under isothermal and non-isothermal conditions show close agreement, indicating that buoyancy effects have minimal influence on the flow field. These distributions, along with tracer studies, form the foundation for the subsequent RTD analysis and

volume partitioning, which are used to assess the mixing efficiency and flow characteristics within the tundish.

Transient tracer injection simulations are performed to characterize the flow behavior. The resulting tracer concentration–time profile, known as the RTD curve, serves as the basis for the RTD-based analysis. Figure 8 shows the RTD curve derived from the CFD simulations, highlighting key metrics such as T_{\min} , T_{\max} , T_{avg} , and T_{th} . The corresponding flow partitioning into plug volume (V_{plug}), mixing volume (V_{mix}), and dead volume (V_{dead}) is illustrated in Figure 9.

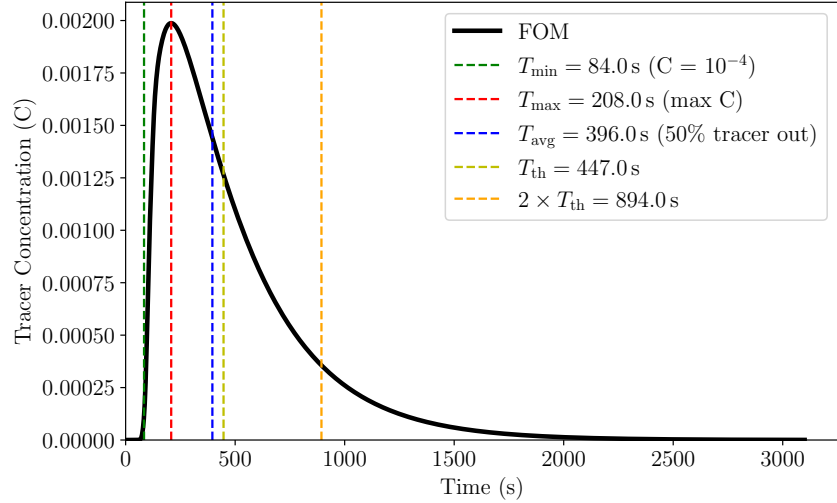


Figure 8: RTD curve derived from FOM simulations, illustrating key flow characteristics required for volume partitioning.

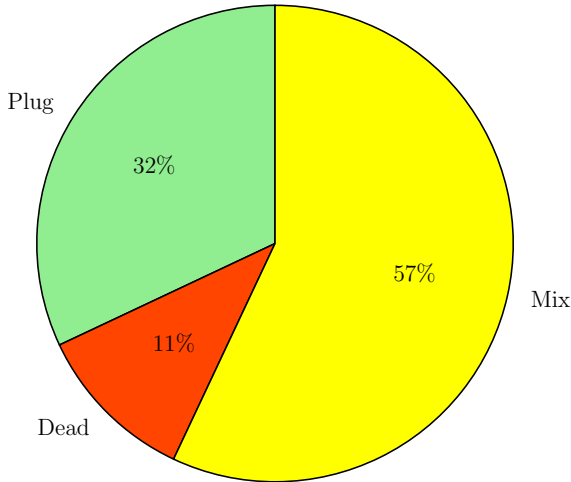


Figure 9: Volume partitioning obtained from RTD analysis of a FOM simulation result.

Table 3 summarizes the inlet velocities and corresponding flow rates considered for the parametric study of RTD behaviour in a single-strand tundish. These cases are used to assess the sensitivity of the RTD characteristics to variations in flow conditions. For each inlet velocity listed in Table 3, an isothermal steady-state simulation is first conducted to compute the velocity field. Subsequently, transient scalar transport simulations are performed to obtain the RTD

curves, shown in Figure 10. As the inlet velocity decreases, the RTD curves broaden, the peak concentration diminishes, and the profiles become increasingly dispersed. This trend reflects the longer residence times and reduced mixing efficiency associated with slower flow rates. The results emphasize the strong dependence of residence time distribution on inlet velocity, with broader RTD curves indicating diminished flow uniformity and reduced system performance.

Parameter No.	Flow rate (m ³ /hr)	Velocity (m/s)
1	36.9365	1.6301
2	34.52985	1.5239
3	32.1232	1.4177
4	29.71655	1.3115
5	27.3099	1.2053
6	24.90325	1.0991
7	22.4966	0.9929
8	20.08995	0.8866
9	17.6833	0.7804
10	15.27665	0.6742
11	12.87	0.5680

Table 3: Inlet velocities and flow rates considered in the parametric study of RTD curves for the single-strand tundish. These parameters were varied to conduct a sensitivity analysis of the RTD characteristics.

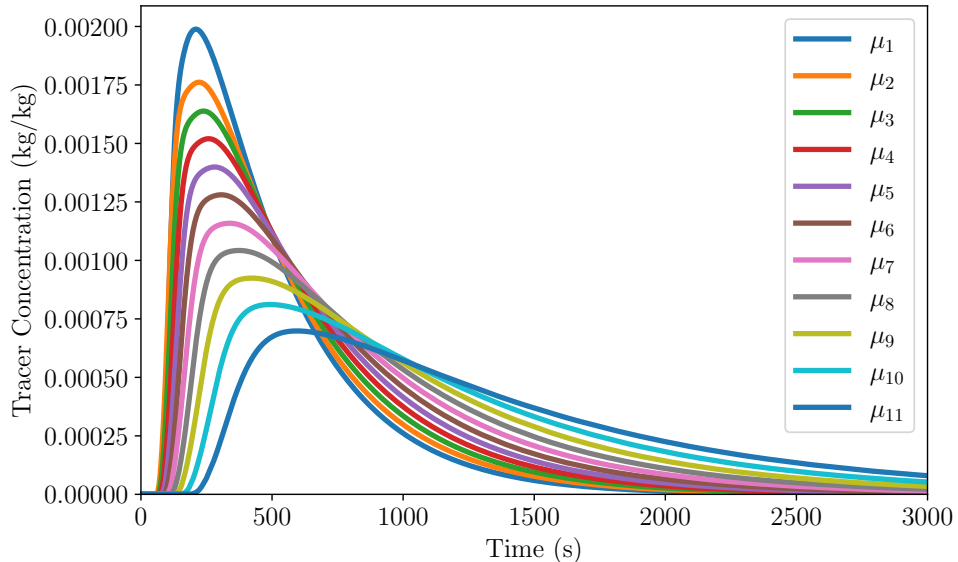


Figure 10: RTD curves obtained from full-order simulations, showing the temporal evolution of tracer concentration at the outlet of the tundish for each parameter listed in Table 3.

To construct the parametric data-driven ROM (see 3) for RTD analysis, we consider parameter values that correspond to distinct simulation cases with varying inlet velocity conditions. Again, we select eight parameter instances — indexed as μ_i , where, $i = \{1, 2, 3, 4, 7, 8, 9, 10\}$, form the training set (from Table 3). The full-order simulation snapshots of these are assembled to build the reduced basis subspace via POD, and to build the mapping from the parameter-time space to the reduced coefficients, RBF interpolation is employed. The remaining parameter instances, μ_i , where, $i = \{5, 6, 11\}$, are for testing. These test parameters are not used during the training phase and serve to evaluate the predictive capabilities and generalization of the ROM,

especially for interpolation and mild extrapolation regimes. POD is performed on the training set, the first 21 modes capturing 99.99% of the cumulative energy are retained to construct the reduced basis subspace.

Figure 11 compares the RTD curves for parameter μ_1 obtained from the experiment (for details about the experiment, readers are referred to the previous work on intrusive projection-based ROM for RTD analysis [7]), the FOM CFD simulation, and the data-driven POD-RBF-ROM. Both the FOM and ROM predictions exhibit good agreement with the experimental data, with only minor discrepancies observed.

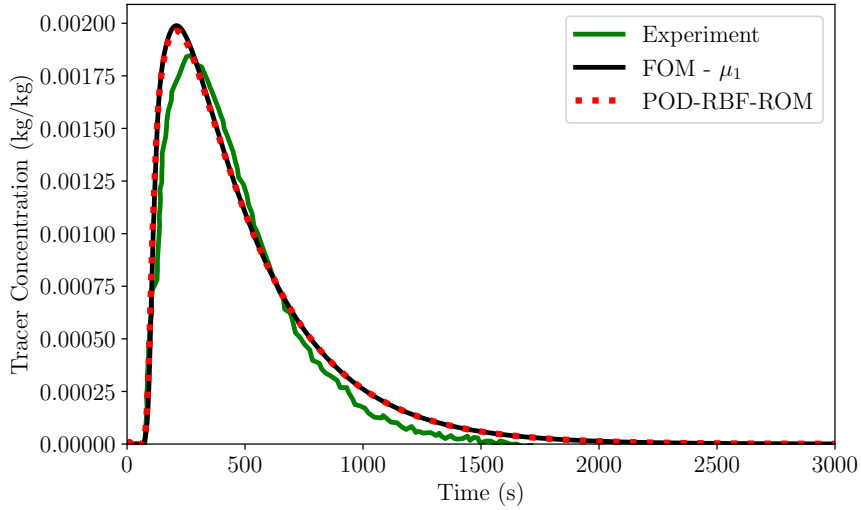


Figure 11: Comparison of RTD curves from the experiment [7], FOM CFD simulation, and data-driven POD-RBF-ROM, illustrating the good agreement between the simulations and experimental data.

In the interpolatory regime, μ_i , where, $i = \{5, 6\}$, the data-driven POD-RBF-ROM shows excellent agreement with the full-order simulation, accurately predicting the RTD curves for test parameters within the range used for training. The model captures the dynamics of the system effectively, providing reliable results for these parameters.

In the extrapolatory regime, where the test parameter μ_{11} is outside the training range, the ROM still captures the overall trend of the RTD curve but shows fluctuations in the initial phase and a slight discrepancy in concentration prediction. This demonstrates the ROM's ability to extrapolate beyond the trained parameters, though with some limitations in precision.

The computational resources and wall-clock time required for the FOM simulations are summarised in Table 4. The computational efficiency achieved using the data-driven ROM for evaluating the QoIs is presented in Table 5. While individual FOM simulations range approximately from 8.19 and 23.17 hours of wall-clock time on 64 to 40 cores, the ROM's online evaluation completes in only 0.33 seconds on a single core, resulting in a speed-up of approximately 1×10^6 faster in wall-clock time compared to the average FOM simulation. Although the ROM offline construction demands around 40 hours on 2 cores, comparable to a single FOM simulation, this cost is a one-time investment, enabling rapid repeated evaluations. This substantial acceleration highlights the ROM's suitability for real-time prediction and optimization tasks.

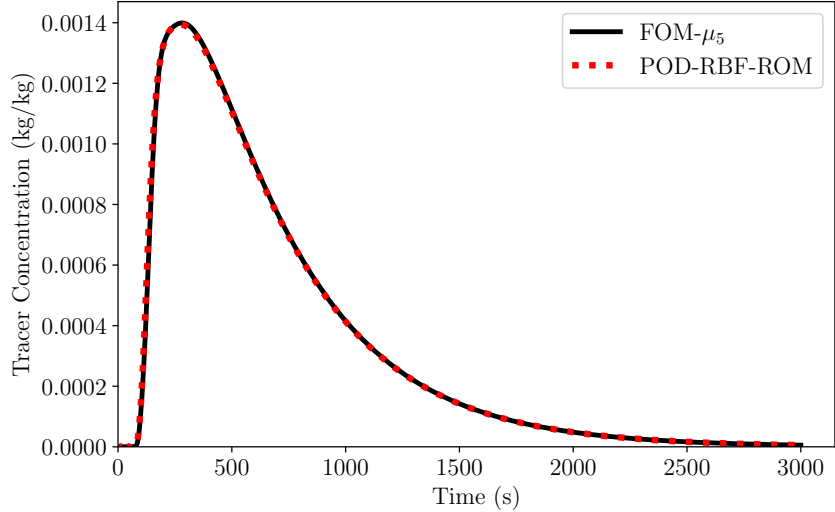


Figure 12: RTD curves for test parameter μ_5 : comparison between the data-driven POD-RBF-ROM and full-order simulation, showing excellent agreement within the interpolatory regime

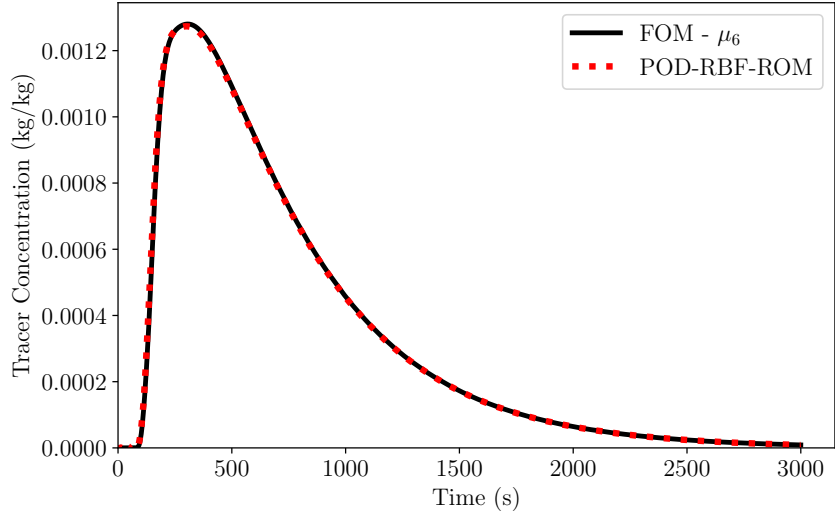


Figure 13: RTD curves for test parameter μ_6 : comparison between the data-driven POD-RBF-ROM and full-order simulation, showing excellent agreement within the interpolatory regime

6 Conclusions and perspectives

Over the last twenty years, mathematical modelling has become a critical approach for analysing flow behaviour in steelmaking tundishes. Given the difficulties associated with conducting experiments in high-temperature environments, physical studies have remained relatively constrained. However, advancements in computational methods have significantly enhanced our ability to study and optimise tundish performance through numerical simulations.

In this work, full-order simulations were conducted under both isothermal and non-isothermal conditions. The findings show that buoyancy effects associated with thermal variations have a negligible impact on the flow field, as the velocity profiles remain nearly identical between the two scenarios. These velocity fields, in conjunction with tracer transport simulations, serve as the foundation for evaluating residence time distribution and volume partitioning. Subsequently, a sensitivity analysis of the RTD curves was conducted by varying the inlet velocities. These re-

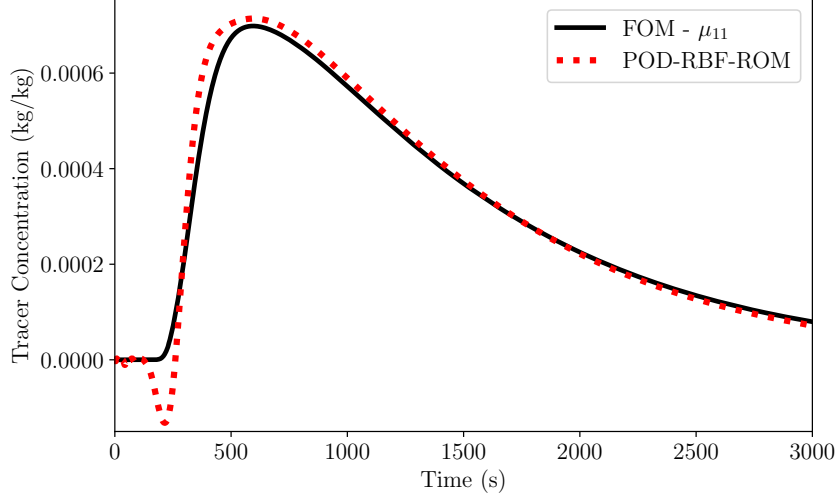


Figure 14: RTD curves for test parameter μ_{11} in the extrapolatory regime: comparison between the data-driven POD-RBF-ROM and full-order simulation, ROM predictions showing fluctuations in the initial phase but accurately capturing the overall trend of the RTD curve, with a slight discrepancy in the concentration prediction.

Expt No.	Wall-clock time	CPU time (core-hours)	Cores Allocated
1	2.81 + 5.38 hours	177.05 + 360 hours	64
2	4.43 + 9 hours	177.2 + 360 hours	40
3	7.26 + 9 hours	283.08 + 360 hours	40
4	6.67 + 9 hours	260.92 + 360 hours	40
5	5.16 + 9 hours	201.55 + 360 hours	40
6	4.24 + 9 hours	165 + 360 hours	40
7	14.17 + 9 hours	555.24 + 360 hours	40
8	3.75 + 9 hours	145.53 + 360 hours	40
9	6.10 + 9 hours	237.70 + 360 hours	40
10	6.54 + 9 hours	256.27 + 360 hours	40
11	10.48 + 9 hours	410.90 + 360 hours	40

Table 4: Summary of computational resources used for the FOM simulations to obtain the tundish steady-state operation QoIs on the Linux cluster. The wall-clock time refers to the elapsed real time, while the CPU time denotes the cumulative usage across all allocated cores (core-hours). These results correspond to the steady Reynolds averaged Navier-Stokes + transient tracer simulations discussed in Table 3.

sults provide a thorough analysis of flow characteristics and mixing efficiency within the tundish.

A comparison of RTD curves obtained from experiments, full-order simulations, and the data-driven ROM indicates close agreement between the model predictions and experimental observations, with only minor discrepancies. This agreement validates the accuracy of the ROM and demonstrates its suitability as a computationally efficient surrogate for full-scale simulations in the analysis of tundish flow behaviour. In the interpolatory regime, the ROM exhibits excellent predictive capability, closely matching the FOM results. In the extrapolatory regime, while the ROM captures the overall shape of the RTD curve, some deviations are observed during the

Data-driven ROM	Offline Wall-clock Time	Offline CPU Time (core-hours)	Online Time (Wall-clock)	Cores Used (Offline / Online)
POD-RBF-ROM	40 hours	80 core-hours	0.33 seconds	2 / 1

Table 5: Computational resources used for the parametric time-dependent data-driven POD-RBF-ROM construction and prediction to obtain the tundish steady-state operation QoIs. The offline phase includes computation of POD modes (whole domain is considered), evaluation of modal coefficients, and RBF regression map construction. The online phase corresponds to the prediction of quantities of interest, the RTD curve at the tundish outlet. The online evaluation is performed only at the outlet probe location, where the QoI is recorded. Evaluating over the entire domain takes approximately 90 seconds, primarily due to the cost of the dot product operation.

initial transient phase.

Future work will focus on extending the framework to more complex industrial scenarios, including multi-outlet tundish configurations. Further refinement is required in the extrapolatory regime, potentially through increasing the training data or via usage of more sophisticated interpolation strategies.

Overall, the integration of ROM techniques significantly reduces computational costs while retaining essential flow characteristics, demonstrating their potential for real-time analysis, design optimization, and digital twin application in metallurgical processes such as continuous casting.

CRediT authorship contribution statement

Harshith Gowrachari: Writing - original draft, Conceptualization, Data curation, Formal Analysis, Investigation, Methodology, Software, Visualization. **Mattia Giuseppe Barra:** Writing – review & editing, Resources, Investigation. **Giovanni Stabile:** Writing – review & editing, Supervision. **Gianluca Bazzaro:** Project administration, Supervision. **Gianluigi Rozza:** Writing – review & editing, Funding acquisition, Project administration, Supervision.

Declaration of Generative AI and AI-assisted technologies in the writing process

These technologies were used to improve readability and correct spelling during the preparation of this manuscript. After using them, the authors reviewed and edited the content as needed and take full responsibility for the content of the publication.

Declaration of competing interest

The authors declare that they have no known competing financial interests or personal relationships that could have appeared to influence the work reported in this paper

Data statement

Access to the data will be unavailable, as the research data includes sensitive and confidential information.

Acknowledgements

We acknowledge the PhD grant supported by industrial partner Danieli & C. S.p.A. and Programma Operativo Nazionale Ricerca e Innovazione 2014-2020, P.I. Gianluigi Rozza. HG gratefully acknowledges Mattia Giuseppe Barra, Gianluca Bazzaro and Gabriele Guastaferro for their valuable discussions and for facilitating the hosting arrangements during multiple visits to Danieli Research Center (DRC). GS acknowledges the financial support under the National Recovery and Resilience Plan (NRRP), Mission 4, Component 2, Investment 1.1, Call for tender No. 1409 published on 14.9.2022 by the Italian Ministry of University and Research (MUR), funded by the European Union – NextGenerationEU – Project Title ROMEU – CUP P2022FEZS3 – Grant Assignment Decree No. 1379 adopted on 01/09/2023 by the Italian Ministry of Ministry of University and Research (MUR) and acknowledges the financial support by the European Union (ERC, DANTE, GA-101115741). Views and opinions expressed are however those of the author(s) only and do not necessarily reflect those of the European Union or the European Research Council Executive Agency. Neither the European Union nor the granting authority can be held responsible for them.

References

- [1] P. Benner, S. Gugercin, and K. Willcox. A survey of projection-based model reduction methods for parametric dynamical systems. *SIAM Review*, 57(4):483–531, Jan. 2015. ISSN 1095-7200. doi: 10.1137/130932715. URL <http://dx.doi.org/10.1137/130932715>.
- [2] A. Bérard, B. Blais, and G. S. Patience. Experimental methods in chemical engineering: Residence time distribution—rtd. *The Canadian Journal of Chemical Engineering*, 98(4): 848–867, Mar. 2020. ISSN 1939-019X. doi: 10.1002/cjce.23711. URL <http://dx.doi.org/10.1002/cjce.23711>.
- [3] L. S. Caretto, A. D. Gosman, S. V. Patankar, and D. B. Spalding. *Two calculation procedures for steady, three-dimensional flows with recirculation*, page 60–68. Springer Berlin Heidelberg, 2007. ISBN 9783540061717. doi: 10.1007/bfb0112677. URL <http://dx.doi.org/10.1007/BFb0112677>.
- [4] C. Chen, G. Cheng, H. Sun, Z. Hou, X. Wang, and J. Zhang. Effects of salt tracer amount, concentration and kind on the fluid flow behavior in a hydrodynamic model of continuous casting tundish. *steel research international*, 83(12):1141–1151, July 2012. ISSN 1869-344X. doi: 10.1002/srin.201200086. URL <http://dx.doi.org/10.1002/srin.201200086>.
- [5] C. Damle and Y. Sahai. The effect of tracer density on melt flow characterization in continuous casting tundishes. a modeling study. *ISIJ International*, 35(2):163–169, 1995. ISSN 0915-1559. doi: 10.2355/isijinternational.35.163. URL <http://dx.doi.org/10.2355/isijinternational.35.163>.
- [6] S. K. Dinda, D. Li, F. Guerra, C. Cathcart, and M. Barati. Continuous casting tundish dead volume study by physical modeling and computational investigation. *steel research international*, 95(11), Sept. 2024. ISSN 1869-344X. doi: 10.1002/srin.202400125. URL <http://dx.doi.org/10.1002/srin.202400125>.
- [7] H. Gowrachari, M. G. Barra, M. Khamlich, G. Stabile, G. Bazzaro, and G. Rozza. Projection-based model order reduction for residence time distribution analysis of an industrial-scale continuous casting tundish, 2025. URL <https://arxiv.org/abs/2509.20366>.

[8] J. Hesthaven and S. Ubbiali. Non-intrusive reduced order modeling of nonlinear problems using neural networks. *Journal of Computational Physics*, 363:55–78, June 2018. ISSN 0021-9991. doi: 10.1016/j.jcp.2018.02.037. URL <http://dx.doi.org/10.1016/j.jcp.2018.02.037>.

[9] J. S. Hesthaven, G. Rozza, and B. Stamm. *Certified Reduced Basis Methods for Parametrized Partial Differential Equations*. Springer International Publishing, 2016. ISBN 9783319224701. doi: 10.1007/978-3-319-22470-1. URL <http://dx.doi.org/10.1007/978-3-319-22470-1>.

[10] B. E. Launder and D. B. Spalding. *Lectures in Mathematical Models of Turbulence*. Academic Press, London and New York, 1972. ISBN 0124380506.

[11] K. Lee and K. T. Carlberg. Model reduction of dynamical systems on nonlinear manifolds using deep convolutional autoencoders. *Journal of Computational Physics*, 404:108973, Mar. 2020. ISSN 0021-9991. doi: 10.1016/j.jcp.2019.108973. URL <http://dx.doi.org/10.1016/j.jcp.2019.108973>.

[12] J. Liu, P. Zhou, X. Zuo, D. Wu, and D. Wu. Optimization of the liquid steel flow behavior in the tundish through water model experiment, numerical simulation and industrial trial. *Metals*, 12(9):1480, Sept. 2022. ISSN 2075-4701. doi: 10.3390/met12091480. URL <http://dx.doi.org/10.3390/met12091480>.

[13] A. Quarteroni, A. Manzoni, and F. Negri. *Reduced Basis Methods for Partial Differential Equations*. Springer International Publishing, 2016. ISBN 9783319154312. doi: 10.1007/978-3-319-15431-2. URL <http://dx.doi.org/10.1007/978-3-319-15431-2>.

[14] Y. Ren, W. Yang, and L. Zhang. Deformation of non-metallic inclusions in steel during rolling process: A review. *ISIJ International*, 62(11):2159–2171, Nov. 2022. ISSN 1347-5460. doi: 10.2355/isijinternational.isijint-2022-235. URL <http://dx.doi.org/10.2355/isijinternational.ISIJINT-2022-235>.

[15] F. Romor, G. Stabile, and G. Rozza. Non-linear Manifold Reduced-Order Models with Convolutional Autoencoders and Reduced Over-Collocation Method. *Journal of Scientific Computing*, 94(3), Feb. 2023. ISSN 1573-7691. doi: 10.1007/s10915-023-02128-2. URL <http://dx.doi.org/10.1007/s10915-023-02128-2>.

[16] G. Rozza, G. Stabile, and F. Ballarin. *Advanced Reduced Order Methods and Applications in Computational Fluid Dynamics*. Society for Industrial and Applied Mathematics, Jan 2022. ISBN 9781611977257. doi: 10.1137/1.9781611977257. URL <http://dx.doi.org/10.1137/1.9781611977257>.

[17] A. Rückert, M. Warzecha, R. Koitzsch, M. Pawlik, and H. Pfeifer. Particle distribution and separation in continuous casting tundish. *Steel Research International*, 80(8):568–574, 2009. doi: 10.2374/SRI09SP043.

[18] Y. Sahai and T. Emi. *Tundish Technology for Clean Steel Production*. WORLD SCIENTIFIC, Dec. 2007. ISBN 9789812790767. doi: 10.1142/6426. URL <http://dx.doi.org/10.1142/6426>.

[19] L. Sirovich. Turbulence and the dynamics of coherent structures. ii. symmetries and transformations. *Quarterly of Applied Mathematics*, 45(3):573–582, Oct. 1987. ISSN 1552-4485. doi: 10.1090/qam/910463. URL <http://dx.doi.org/10.1090/qam/910463>.

[20] G. Stabile and G. Rozza. Finite volume pod-galerkin stabilised reduced order methods for the parametrised incompressible navier–stokes equations. *Computers & Fluids*, 173:

273–284, Sept. 2018. ISSN 0045-7930. doi: 10.1016/j.compfluid.2018.01.035. URL <http://dx.doi.org/10.1016/j.compfluid.2018.01.035>.

[21] G. Stabile, F. Ballarin, G. Zuccarino, and G. Rozza. A reduced order variational multiscale approach for turbulent flows. *Advances in Computational Mathematics*, 45(5–6):2349–2368, June 2019. ISSN 1572-9044. doi: 10.1007/s10444-019-09712-x. URL <http://dx.doi.org/10.1007/s10444-019-09712-x>.

[22] G. Stabile et al. ITHACA-FV: In real Time Highly Advanced Computational Applications for Finite Volumes - ROMs for OpenFOAM. <https://github.com/ithaca-fv/ITHACA-FV>, 2025.

[23] T. Taddei. A Registration Method for Model Order Reduction: Data Compression and Geometry Reduction. *SIAM Journal on Scientific Computing*, 42(2):A997–A1027, Jan. 2020. ISSN 1095-7197. doi: 10.1137/19m1271270. URL <http://dx.doi.org/10.1137/19M1271270>.

[24] M. Tezzele, N. Demo, G. Stabile, and G. Rozza. *Chapter 9: Nonintrusive Data-Driven Reduced Order Models in Computational Fluid Dynamics*, page 203–222. Society for Industrial and Applied Mathematics, Jan. 2022. ISBN 9781611977257. doi: 10.1137/1.9781611977257.ch9. URL <http://dx.doi.org/10.1137/1.9781611977257.ch9>.

[25] M. Tkadlečková, J. Walek, K. Michalek, and T. Huczala. Numerical analysis of rtd curves and inclusions removal in a multi-strand asymmetric tundish with different configuration of impact pad. *Metals*, 10(7):849, June 2020. ISSN 2075-4701. doi: 10.3390/met10070849. URL <http://dx.doi.org/10.3390/met10070849>.

[26] Q. Wang, C. Tan, A. Huang, W. Yan, H. Gu, Z. He, and G. Li. Numerical simulation on refractory wear and inclusion formation in continuous casting tundish. *Metallurgical and Materials Transactions B*, 52(3):1344–1356, 2021. ISSN 1543-1916. doi: 10.1007/s11663-021-02097-7. URL <http://dx.doi.org/10.1007/s11663-021-02097-7>.

[27] Z. Wang, Z. Yang, X. Wang, Q. Yue, Z. Xia, and H. Xiao. Residence time distribution (rtd) applications in continuous casting tundish: A review and new perspectives. *Metals*, 12(8):1366, Aug. 2022. ISSN 2075-4701. doi: 10.3390/met12081366. URL <http://dx.doi.org/10.3390/met12081366>.

[28] H. G. Weller, G. Tabor, H. Jasak, and C. Fureby. A tensorial approach to computational continuum mechanics using object-oriented techniques. *Computers in Physics*, 12(6):620–631, Nov. 1998. ISSN 0894-1866. doi: 10.1063/1.168744. URL <http://dx.doi.org/10.1063/1.168744>.

[29] World Steel Association. World steel in figures 2024, 2024. URL <https://worldsteel.org/wp-content/uploads/World-Steel-in-Figures-2024.pdf>.

[30] D. Xiao, F. Fang, C. Pain, and G. Hu. Non-intrusive reduced-order modelling of the navier–stokes equations based on rbf interpolation. *International Journal for Numerical Methods in Fluids*, 79(11):580–595, July 2015. ISSN 1097-0363. doi: 10.1002/fld.4066. URL <http://dx.doi.org/10.1002/fld.4066>.

[31] L. Zhang and B. G. Thomas. Inclusions in continuous casting of steel. In *Proceedings of the XXIV National Steelmaking Symposium*, pages 184–198, Morelia, Michoacán, Mexico, November 26–28 2003. URL https://ccc.illinois.edu/PDF%20Files/Presentations/03_Inclusions_in_Continuous_Casting_of_Steel.pdf.

[32] L. Zhang, Q. Ren, H. Duan, Y. Ren, W. Chen, G. Cheng, W. Yang, and S. Sridhar. Modelling of non-metallic inclusions in steel. *Mineral Processing and Extractive Metallurgy*, 129(2):184–206, Mar. 2020. ISSN 2572-665X. doi: 10.1080/25726641.2020.1738087. URL <http://dx.doi.org/10.1080/25726641.2020.1738087>.